Düzce University
Journal of Science & Technology

Research Article

Investigation of Electromagnetic Shielding Performance of Monolayer Ironboride in Tetragonal Crystal Structure using Ab initio Methods

Hakan ÜŞENTİ [a,*], İzzet Paruğ DURU [b]

[a] *Department of Electricity and Energy, Düzce Vocational School, Düzce University, Düzce, TURKEY*
[b] *Department of Medical Imaging, Gedik Vocational School, İstanbul Gedik University, İstanbul, TURKEY*
** Corresponding author's e-mail address: hakanusenti@duzce.edu.tr*
DOI: 10.29130/dubited.1618327

ABSTRACT

The negative effects of pollution caused by electromagnetic radiation on human health and sensitive systems have reached serious dimensions. The most effective way to deal with this pollution is to create isolated areas with shielding materials. Especially after the discovery of graphene, studies on 2D materials continue to reveal the extraordinary structural, electronic, and optical properties of 2D materials. Thanks to the research on the use of monolayer materials in electromagnetic shielding, ultra-thin, and high-performance shielding materials are being obtained. In this study, the electromagnetic radiation shielding efficiency (SE) of a 2D film-structured material with a tetragonal crystal structure in the MBenes class of the MXene family and obtained using Fe_2B unit cells in the P4/mmm space group has been investigated using ab initio methods. The electrical, optic, and magnetic behavior of the material in the ground state is determined using the density functional theory (DFT) approach. The Curie temperature was investigated using the Monte Carlo method. The shielding efficiency of Fe_2B has been investigated in the range of 31.558-123980 nm of the electromagnetic wave spectrum at [001], [010], [100] polarization states. Despite Fe_2B 2D monolayer film structure, it showed a shielding performance (SE_T) of >20 dB. This study shows that Fe_2B in film structure is a promising and exciting material for ultra-thin shielding material applications with its superior shielding performance at nanometer dimensions.

Keywords: *Ab initio, DFT, shielding effect, MBenes, Fe_xB_y*

Tetragonal Kristal Yapıdaki Tek Katmanlı Demirborürün Elektromanyetik Kalkanlama Performansının Ab initio Yöntemler Kullanılarak İncelenmesi

ÖZ

Elektromanyetik radyasyonun neden olduğu kirliliğin insan sağlığı ve hassas sistemler üzerindeki olumsuz etkileri ciddi boyutlara ulaşmıştır. Bu kirlilik ile başa çıkabilmenin en etkili yolu kalkanlama malzemeleri ile izole edilmiş alanlar yaratmaktır. Özellikle grafenin keşfinden sonra 2D malzemeler üzerine yapılan çalışmalar ile 2D malzemelerin olağan üstü yapısal, elektronik ve optik özellikleri hale keşfedilmeye devam etmektedir. Monolayer malzemelerin elektromanyetik kalkanlama alanında kullanılması amacıyla yapılan araştırmalar sayesinde ultra ince ve yüksek performanslı kalkanlama malzemeleri elde edilmeye çalışılmaktadır. Bu çalışmada MXene ailesine ait MBenes sınıfında bulunan tetragonal kristal yapıya sahip ve P4/mmm uzay grubunda bulunan Fe_2B birim hücreleri kullanılarak elde edilmiş olan film yapılı 2D malzemenin

Received: 12/01/2025, Revised: 14/02/2025, Accepted: 24/02/2025

elektromanyetik radyasyonu kalkanlama etkililiği (SE); ab initio yöntemler kullanılarak araştırılmıştır. Malzemenin taban durumundaki elektriksel ve manyetik davranışı yoğunluk fonksiyonel teorisi (DFT) yaklaşımı kullanılarak belirlenmiştir. Curie sıcaklığı Monte Carlo Metodu kullanılarak araştırılmıştır. Fe_2B'nin kalkanlama etkililiği elektromanyetik dalga spektrumunun 31.558-123980 nm aralığında [001], [010], [100] polarizasyon durumlarında incelenmiştir. Fe_2B 2D monolayer film yapısına rağmen >20 dB seviyesinde kalkanlama performansı (SE_T) göstermiştir. Bu çalışma göstermiştir ki; film yapıdaki Fe_2B, nanometre boyutlarındaki üstün kalkanlama performansı ile ultra ince kalkanlama malzemesi uygulamaları için umut ve heyecan verici bir malzemedir.

Anahtar Kelimeler: *Ab initio, DFT, kalkanlama etkisi, MBenes,* Fe_xB_y

I. INTRODUCTION

The electric field and the magnetic field are the two main components of electromagnetic pollution (radiation) that can be measured. Radiation emitted as waves or particles comes in two basic types. One of these is ionizing radiation, which has a certain mass and energy, can move rapidly, and can be in the form of particles or electromagnetic waves such as alpha, beta, and neutron radiation, and the other is high-energy radiation that reacts with the nucleus or orbits by affecting the atom it encounters [1-3]. Gamma and X-rays in the form of electromagnetic waves are massless radiation types. Radio waves, infrared waves, ultraviolet light, and microwaves are low-energy nonionizing electromagnetic waves that do not cause any change in the nuclei and orbits of the atoms they encounter [1, 2].

The main electromagnetic field generators are electrically powered devices, current-carrying conductors, high-voltage lines, radio-TV transmitters, microwave ovens, Wi-Fi access systems, energy-saving light bulbs, and devices used for industrial and medical diagnostics. Wireless telecommunication systems, which have become widespread, especially since the 1990s, have become the main actor of electromagnetic radiation generation. At the same time, the use of new technologies such as the Internet of Things (IoT) and 5G is causing new radio frequencies to emerge and this pollution to increase even faster. The widespread use of these electromagnetic pollution-causing radiation generators, even in rural areas, has led to a large increase in electromagnetic pollution due to population density. This pollution appears as the sum of the radiation pollution emitted by many electromagnetic wave generators. This summation effect of electromagnetic pollution causes increasing environmental pollution that grows day by day [4-7].

Electromagnetic radiation (EMR), which we are exposed to in our daily lives, has two basic components: very low frequency (ELF) band (<300 Hz) produced by electrical devices, high voltage lines and transformers, and radio frequency (RF) and microwave (MW) with high frequency from 3 kHz to 300 GHz from base stations, cell phones, radio and TV transmitters [3, 6, 8].

Human-induced environmental pollution ("electrosmog"), which has increased most rapidly in recent years, not only threatens our health depending on the duration and severity of exposure but also has negative effects on sensitive systems, such as disruption of stable operation and interference [5, 6, 9-11]. When the electromagnetic wave (EMW) we are exposed to in our living spaces against our will hits the tissue surface, some of it is reflected but the rest is absorbed by the body. Prolonged exposure to electromagnetic waves that produce a thermal effect on the tissue causes tissue damage. If the field strength of the wave cannot create the friction that can generate heat in the tissue, charges that are in motion in a continuous electric field such as ions, molecular dipoles, and colloid particles are also exposed to non-thermal effects. Depending on the nature of the organism, non-thermal effects can be stronger than thermal effects. The International Agency for Research on Cancer (IARC) identified ELF-type magnetic fields as a class 2B carcinogen in October 2001, and the World Health Organization (WHO) announced in 2004 that ELF magnetic fields increase childhood leukemia by a factor of two. In addition to the short-term effects of electromagnetic fields such as stress, insomnia, migraine, skin problems, memory loss, and weight gain, many scientific studies have proven that long-

term exposure to electromagnetic fields can cause leukemia, brain tumors, heart disease, Parkinson's, Alzheimer's, cancer, increased risk of miscarriage during pregnancy, as a result of their effects on molecular and chemical bonds, cell structure and immune system [3, 8, 11, 12].

The most effective way to deal with electromagnetic radiation is to create isolated areas using materials called “electromagnetic shielding” that can block the interference of radiation. Shielding materials should have properties that can meet the needs of different sectors. Studies on the production and application of shielding materials with these properties are still ongoing [13-17].

The shielding strategy is based on absorption, reflection, and multiple internal reflections of the electromagnetic wave within the shielding material. The electromagnetic wave interacting with the monolayer shielding material utilizes the impedance mismatch between the shield and the air, reflecting part of the EMW from the surface and dissipating the rest by absorption as heat energy inside the shield. In the inner thickness of the shield, the effect of secondary reflections and refractions is mostly negligible, since it has a very small effect compared to the main reflection and absorption effect. This reduces the effect of the wave penetrating the shield. The amount of this reduction is determined by the shielding efficiency (SE) parameters and is expressed in decibels (dB) [6, 10, 11, 15].

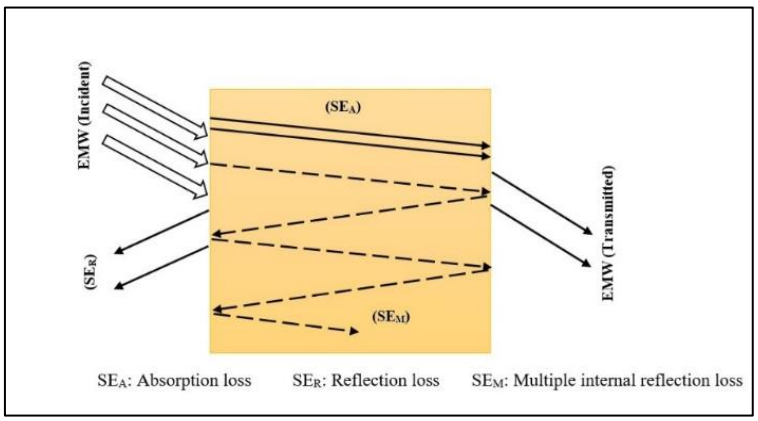

Figure 1. *Schematic representation of the EMI shielding mechanism*

The SE value, which varies with frequency, is calculated by the formula in Equation 1. As seen in the formula, the shielding effect is determined as the logarithmic ratio of the power (P) transmitted to and from the shield [11, 18, 19].

$$SE_T(dB) = 10log\frac{PT}{PI} = 20log\frac{ET}{EI} \quad (1)$$

The total shielding effectiveness (SE_T) is the sum of the shielding effect due to reflection (SE_R), the shielding effect due to absorption (SE_A), and the shielding effect due to multiple internal reflections (SE_M) as stated in Schelkunoff's theory.

$$SE_T(dB) = SE_R(dB) + SE_A(dB) + SE_M\,(dB) \quad (2)$$

Neglecting the SEM, which has a very small effect, the total shielding effect becomes as shown in Equation 3.

$$SE_T(dB) = SE_R(dB) + SE_A(dB) \quad (3)$$

The synthesis and fabrication of shielding materials that are corrosion-resistant, lightweight, flexible, easy to process, inexpensive, and capable of high SE performance is a popular research topic today [20].

To exhibit electromagnetic shielding behavior, a material must exhibit good electrical conductivity at frequencies greater than 300 MHz. Materials with high conductivity can reduce the electric component (E) and the magnetic component (H) simultaneously. However, when the frequency is less than 30 MHz, only ferromagnetic materials are capable of reducing the magnetic component (H) [11].

Mu-metals, carbon derivatives (carbon black, carbon fiber, graphite, and graphene), polymer composites, conducting polymers, intrinsically conducting polymers (IPC), and nanocomposites have been frequently used for electromagnetic shielding. Although they have good shielding performance, metals, and carbon derivatives are not preferred as shielding materials in industrial applications and scientific studies because they have disadvantages such as brittleness, low impact resistance, and corrosion, as well as advantages such as cheapness and easy processability. Although they exhibit suitable behavior as shielding materials, carbon black, carbon fiber, graphite, and graphene (except for some graphite derivatives) are disadvantaged because they need a carrier phase to increase their resistance to external factors. Nanocomposites have become popular over metals as shielding materials due to their advantages such as light weight, flexibility, corrosion resistance, and ease of application [12, 15, 19-23].

Graphene, which was synthesized as a monolayer by Kostya et al. in 2004, is a transition to planar two-dimensional (2D) materials. After the synthesis of graphene, which was very difficult to synthesize due to its thermodynamic instability, the quantum phenomena (massless Dirac fermions, anomalous quantum hall effect, Klein's paradox) in its physical and chemical properties are remarkable. Due to these properties, the discovery of graphene is a breakthrough in the discovery of 2D monolayer materials [24].

The most interesting additions to the discovery and fabrication process of 2D materials are transition metal carbides, nitrides and carbonitride structures (i.e. MXenes). Atomic-layered MXenes are obtained by selectively etching MAX phases from their bulk-layered parents. In MAX phases, named according to their composition, M is a transition metal, A is an element mostly found in columns 3A and 4A, and X is carbon (C) or nitrogen (N) [25, 26]. All MBene, which can be obtained by selective removal of A atomic layers (A is often aluminum) in MAB phases, exhibit good metallic properties with high electron transfer efficiency. M in the MBene structure represents a transition metal and B represents a boron [27, 28].

Two-dimensional (2D) transition metal borides, called MBenes, are derived from the ternary boride group. The performance of boron (B) in 2D materials was discovered thanks to MBenes. A practical way to obtain boron-based 2D materials is to use boron and one of several transition metals. In this case, the transition metal donates electrons to boron to stabilize the boron layer, while at the same time, the transition metal contributes to the diversity of 2D boride materials in a centrally coordinated manner [27]. The use of 2D materials in the synthesis of ultra-thin, lightweight, widely applicable, high-performance shielding materials is the most current area of research.

In recent years, the design of Fe-containing nanostructures has greatly increased. This is due to the many advantages of nanoscale structures such as high aspect ratio, porosity, and high magnetic moment (superparamagnetic behavior) compared to bulk structures. In this study, the SE performance of MXene/MBene family member, Fe_xB_y, a 2D monolayer material (Fe_2B) with a tetragonal crystal structure and P4/mmm space group in 2D monolayer structure, has been theoretically investigated in detail with quantum mechanical based DFT approach using ab initio methods.

II. MATERIAL-METHOD

In this study, the electromagnetic shielding efficiency of 2D film-structured Fe_2B with a tetragonal crystal structure in the P4/mmm space group was investigated.
The lattice parameters of the Fe_2B unit cell are shown in Table 1; the lattice parameters are a=3.494 Å, b=3.494 Å, and c=2.507 Å; the angles are α=90.000°, β=90.000°, γ=90.000°. The unit cell volume of Fe_2B is V=30.605 $Å^3$.

Table 1. *Lattice parameters of Fe_2B unit cell with tetragonal crystal structure.*

Material Name	**Lattice parameters** (Å)	**Unit cell angles** (˚)	**Unit cell volume and density**
Fe_2B (P4/mmm)	a = 3.494 b = 3.494 c = 2.507	α = 90.000° β = 90.000° γ = 90.000°	V=30.605 $Å^3$ d=6.650 gr/cm^3

The structural, electrical, and optical properties of Fe_2B, which is stable in the ferromagnetic (FM) state, have been calculated using the Generalized Gradient Approximation (GGA) [29] and the Perdev-Burke-Ernzerhov (PBE) functional [30]. In these calculations, the CASTEP software package [31], which uses a quantum mechanical background and is capable of performing ab initio computational approaches within the framework of Density Functional Theory (DFT) [32], was used. Geometry Optimization calculations using the LBFGS algorithm were performed using OTFG Ultrasoft pseudopotentials. K points were obtained by setting the Monkhorst-Pack grid to 9X9X12. The Koelling-Hormon correction cut-off plane wave basis set for the SCF in the PBE work flux was set to 353.70 eV. The SCF tolerance was $1.0X10^{-6}$ eV $atom^{-1}$, the maximum force was 0.03 eV $Å^{-1}$, the maximum stress was 0.05 GPa and the maximum displacement tolerances were $1.0X10^{-3}$ Å. Since the parameters used in the geometry optimization were similar to those used in the energy calculations, the energy cutoff was set to 390 eV and the SCF tolerance was set to $1.0X10^{-7}$ eV $atom^{-1}$.

The optical behavior of Fe_2B is characterized by the real ($\varepsilon^{\prime}$) and imaginary ($\varepsilon^{\prime\prime}$) parts of the dielectric function ($\varepsilon(\omega)$), which vary with the frequency of the incident photon. The optical behavior of the material also reveals its SE performance. The relationship between the real ($\varepsilon^{\prime}$) and imaginary parts ($\varepsilon^{\prime\prime}$) of the dielectric function and the optical behavior can be seen in the following equations.

$$n(\omega) = \left[\frac{\sqrt{\varepsilon^{\prime 2}(\omega)+\varepsilon^{\prime\prime 2}(\omega)}+\varepsilon^{\prime}(\omega)}{2}\right]^{\frac{1}{2}} \quad (3)$$

$$k(\omega) = \left[\frac{\sqrt{\varepsilon^{\prime 2}(\omega)+\varepsilon^{\prime\prime 2}(\omega)}-\varepsilon^{\prime}(\omega)}{2}\right]^{\frac{1}{2}} \quad (4)$$

$$\alpha(\omega) = \frac{\omega\sqrt{2}}{c}\left[\sqrt{\varepsilon^{\prime 2}(\omega)+\varepsilon^{\prime\prime 2}(\omega)}-\varepsilon^{\prime}(\omega)\right]^{\frac{1}{2}} \quad (5)$$

$$R(\omega) = \frac{(n(\omega)-1)^1+k^2(\omega)}{(n(\omega)+1)^1+k^2(\omega)} \quad (6)$$

In the above equations, the refractive index is represented as n(ω), the extinction coefficient k(ω), absorption α(ω) and reflection R(ω). Since the combined effect of absorption-induced shielding (SE_A) and reflection-induced shielding (SE_R) gives the total shielding efficiency (SE_T), the relationship between the optical character of the material and the SE efficiency is shown in Equation 9.

$$SE_A(dB) = 10log\left(\frac{1-R}{T}\right) \quad (7)$$

$$SE_R(dB) = 10log\left(\frac{1}{1-R}\right) \quad (8)$$

$$SE_T(dB) = SE_A(dB) + SE_R(dB) = 10log\left(\frac{1}{T}\right) \quad (9)$$

The unit cell structure of Fe_2B was visualized using the lattice parameters using the VESTA package program [33] as shown in Figure 2.

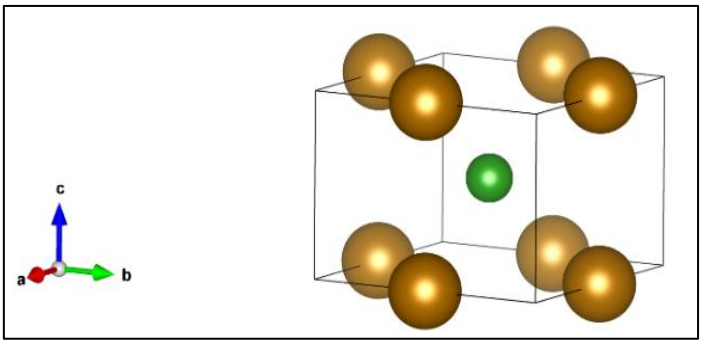

Figure 2. *Fe_2B unit cell (atoms in yellow represent Fe and atoms in green represent B atoms)*

The a, b, and c perspectives of the mesh structure formed using the obtained Fe_2B unit cell structure are shown in Figure 3.

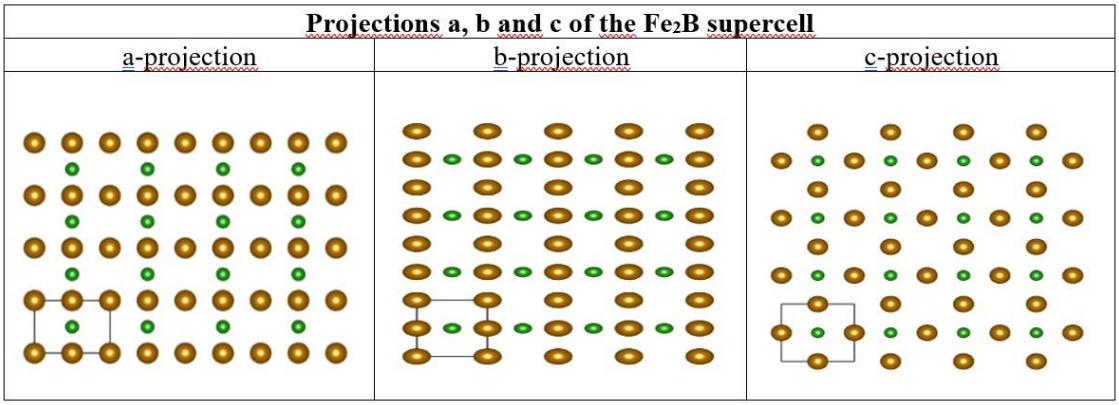

Figure 3. *Representation of Fe_2B supercells obtained using unit cells in the form of a, b and c projections*

The bond lengths and bond angles of the obtained unit cell Fe_2B determined its atomic morphology and also provided information about its magnetic and electronic properties and thus its SE behavior. Using the Kohn-Sham method, DFT was used to look at the kinetic energy and electron density in the

orbitals, and PBE, a popular GGA functional, was used to determine the relationship between the electron density and the energy function.

III. DETERMINATION OF ELECTRONIC, MAGNETIC, OPTICAL PROPERTIES OF Fe_2B

A. ELECTRONIC AND MAGNETIC CHARACTERISTICS

By calculating the density of states and band structure, information about the electronic and magnetic properties of Fe_2B was obtained. It is observed that the total energy and DOS calculations give consistent results for the Blöch correction and tetrahedron method. In addition, the major and minor channels in the band structure were obtained in the spin-polarized state. The band gap was created by using the valence band maximum (VBM) and conduction band minimum (CBM) so that the metallic behavior of Fe_2B could be observed. Figure 4 shows the electronic band structure of Fe_2B, which exhibits ferromagnetic behavior, obtained using major and minor spin channels with the Fermi level set to zero.

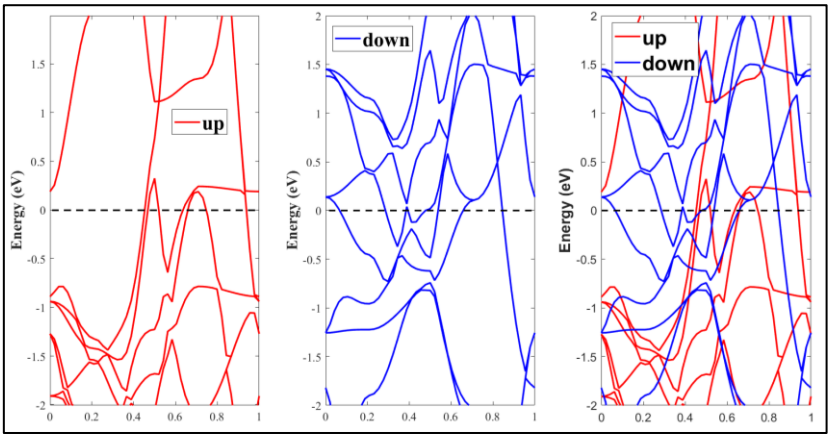

Figure 4. *Electronic band structure of Fe2B in the FM state tuned to the Fermi level*

When the band structure is examined, the conduction and valence bands, which overlap in places to create a minimum energy difference, show that Fe_2B exhibits metallic behavior. At the same time, the up and down-oriented spin state reveals that Fe_2B, which exhibits metallic behavior, also avoids semi-metallic behavior.

Partial density of states (PDOS) plots were used to obtain information about the magnetic properties and electronic structure of the material. Figure 5. shows the PDOS of ferromagnetic Fe_2B and the TDOS graph obtained from their summation.

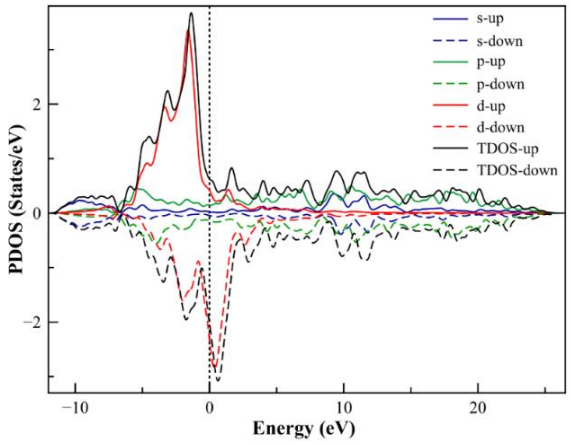

Figure 5. *Partial density of states (PDOS) and density of states (TDOS) of Fe_2B in the FM state*

Figure 5. shows the presence of magnetization caused by the hybridization of the p orbitals of Boron and d orbitals of Iron in the region close to the Fermi level. In this way, the material exhibits FM behavior.

Orbital hybridization, direct or indirect exchange interactions, charge transport, and spin orientations are important physical properties determined by the bond lengths and angles between atoms. According to crystal field theory (CFT), it is possible to divide the d-orbital into a high-energy region (e_g) and a low-energy region (t_{2g}) [34].

To clarify the energy difference between t_{2g} and e_g, the structures containing transition elements can be examined by removing the degeneracy in the d-orbital. Thus, by looking at the electron placement in the orbitals, information about the unpaired spin and the total magnetic moment can be obtained.

Heisenberg Hamiltonian is considered to elaborate magnetic feature of Fe_2B. It is given by Equation 10.

$$H = \frac{1}{2}\sum_{\substack{i,j \\ i \neq j}} J_{ij} S_i . S_j \tag{10}$$

J_{ij} denotes the Exchange energy between i and j indices, while S_i and S_j are the spin value of the choosen spin. The authors generate supercell of Fe_2B in 100x100x2 size from DFT optimized unitcell. Expectation values of thermodynamic quantities, observables as magnetic susceptibility and temperature related magnetization are calculated via Monte Carlo Simulation Method. A classic MCS procedure is applied starting by a randomized spin configuration and zero magnetic field. 60% of total Monte Carlo Steps are used to reduce fluctuations. The rest stands for measurement. Unnecessary MCS moves may increae spin-spin correlations. Therefore, total MCS number as 10E8 and the percentages are determined after several trials. Note that exchange constants of $J_{Fe\text{-}Fe}$ are derived from DFT calculations ($\Delta E = E_{FM} - E_{AFM}$). Markov Chain Monte Carlo scheme in Metropolis algorithm is preferred satisfying detailed balance condition. The codes are written in C programming language by the authors. Susceptibility (χ) and average magnetization (M) vs temperature (T) are calculated via Equation 11 and Equation 12 to point out the Curie temperature.

$$M = \frac{\sum_{i=1}^{N} S_i}{N} \tag{11}$$

$$\chi = \beta(\langle M^2 \rangle - \langle M \rangle^2) \tag{12}$$

Figure 6. shows the magnetic susceptibility and Curie temperature for Fe_2B.

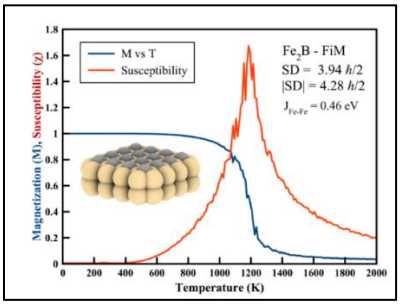

Figure 6. *Magnetization (M), Susceptibility (χ) and Curie temperature (T_c) for Fe2B exhibiting ferrimagnetic (FiM) behavior (Fe-Fe exchange interaction energy (J_{Fe-Fe}) 0.46 eV; Cruie temperature (T_c) 1200K; spin density (SD) 3.94 ħ/2)*

Thanks to the morphological properties of the material and the hybridization in the orbitals, information about the structural and magnetic properties of Fe_2B has been obtained. In addition, as shown in Figure 6. the Fe-Fe exchange interaction energy (J_{Fe-Fe}) was found to be 0.46 eV as a result of the ground state energy calculations performed for Fe_2B by considering the unit cell structure of iron (Fe) in the temperature-varying bcc model. The magnetic dipole moment per unit volume, i.e. the magnetization (M) of Fe_2B decreased dramatically in the range of 1000K-1400K, starting from 1A/m at 0K and including the Cruie temperature (T_c=1200K). If we look at the magnetic susceptibility (χ) of Fe_2B, we see that it increases from 0K up to the Curie temperature of 1200K and then decreases at the same rate. In light of this information, it is seen that Fe_2B exhibits ferrimagnetic (FiM) character as magnetic behavior.

B. ENERGY CALCULATIONS: DIELECTRIC FUNCTION AND OPTICAL PROPERTIES

The ferromagnetic (FM) state of Fe_2B is investigated using the Perdev-Burke-Ernzerhov (PBEsol) functional and the generalized gradient approximation (GGA). The absorption, reflection, and transmission coefficients of the material are calculated using the dielectric tensor obtained by calculating the frequency-dependent dielectric function. Figure 7. Energy dependence of the real (ε^{I}) and imaginary (ε^{II}) parts of the dielectric function ε(ω) in the material depending on the direction of photon incident ([001], [010] and [100]) on Fe_2B in the FM state.

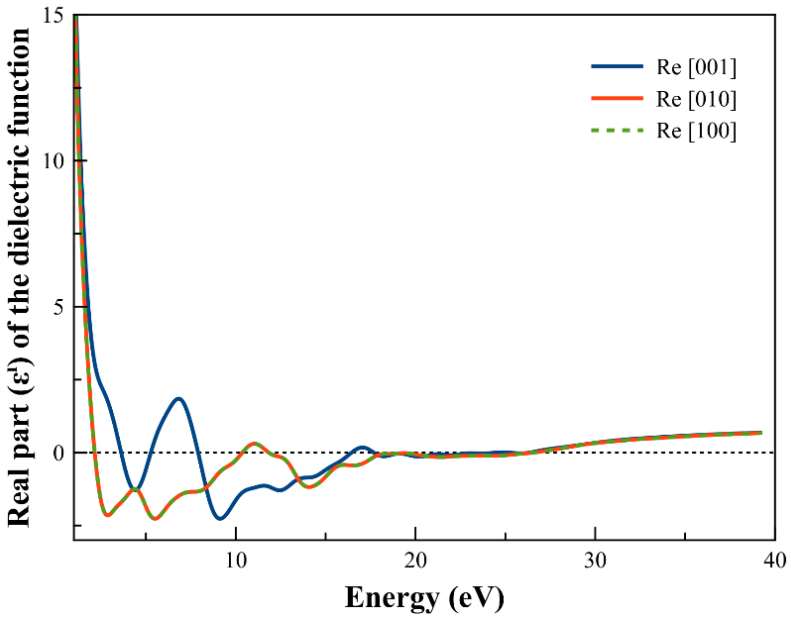

***Figure 7**. Variation of the real (ε') part of the dielectric function with photon energy for polarization states [001], [010] and [100]*

As seen in Figure 7, when the effect of the photon on the real part (ε') of the dielectric function of Fe_2B in the polarization states [001], [010] and [100] is examined, it is observed that they exhibit similar behavior and take the same values in the polarization states addressed as [010] and [100], while a divergent behavior emerges in the polarization state indicated by [001]. The static dielectric behavior they exhibited at frequency values close to zero became dynamic after ~3 eV and continued to react inversely to radiation up to ~27 eV. The real part (ε'), which is responsible for the stored energy, was particularly affected by the electric field, one of the components of the polarized electromagnetic wave, and showed a relaxation frequency characteristic. After ~27 eV, it becomes more stable, taking a positive value for all cases. After the energy level of ~27 eV, Fe_2B continued to produce the same ε' value for the photon polarization states addressed by [001], [010] and [100].

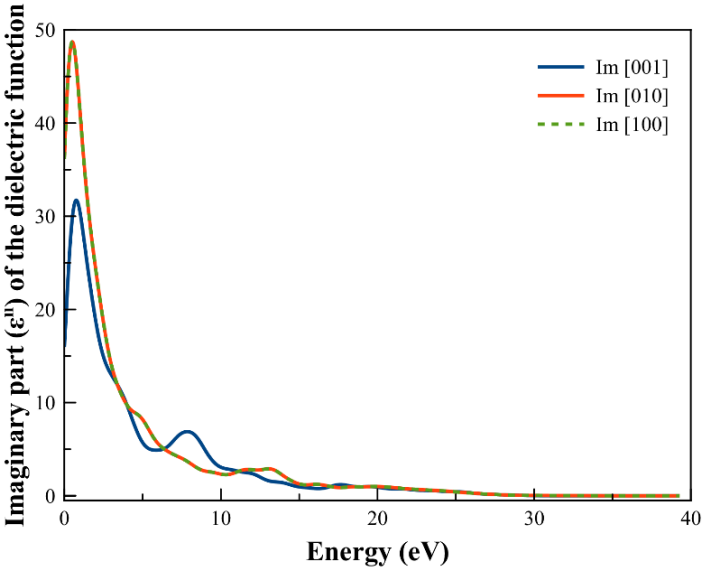

***Figure 8**. Variation of the imaginary (ε'') part of the dielectric function with photon energy for polarization states [001], [010] and [100]*

As seen in Figure 8, when the effect of changing photon energy on the virtual part of the dielectric function (ε^{II}) of Fe_2B in the polarization states [001], [010] and [100] is examined, it is seen that they exhibit similar behavior in the polarization states addressed as [010] and [100], while a divergent behavior emerges in the polarization state indicated by [001]. As it is known, the virtual part of the dielectric function (ε^{II}) is responsible for the energy losses, i.e. the attenuation of the photon wave. Up to an energy level of ~1 eV (corresponding to the infrared region), ε^{II} is increased, which is also the region where the absorption effect is increased. However, after this energy level, the ε_I value starts to decrease dramatically and this effect lasts until the energy level of ~15 eV. Figure 9 shows the photon energy dependence of the absorption coefficient ($\alpha(\omega)$), extinction coefficient ($k(\omega)$), energy-loss function ($L(\omega)$), and refractive index ($n(\omega)$), which determine the optical properties of Fe_2B, for polarization states [001], [001] and [100].

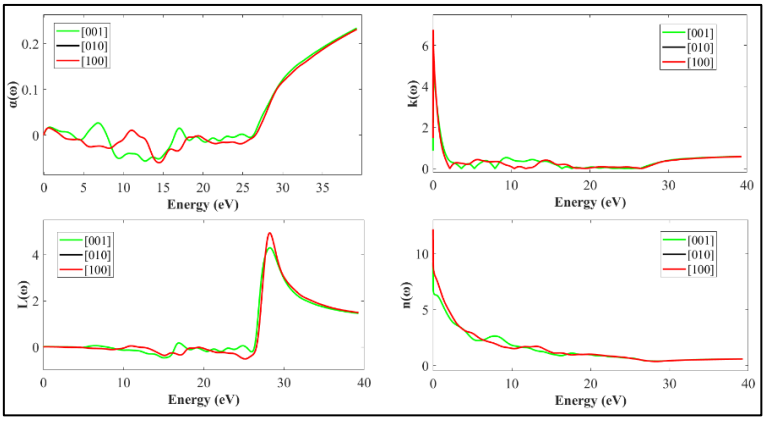

Figure 9. *Photon energy dependence of the absorption coefficient (α(ω)), extinction coefficient (k(ω)), energy-loss function (L(ω)), and refractive index (n(ω)), which determine the optical properties of Fe_2B, for polarization states [001], [001] and [100]*

The photon energy-dependent change in the optical properties of Fe_2B is shown in Figure 9. For polarization states [001], [001] and [100]; absorption coefficient ($\alpha(\omega)$), extinction coefficient ($k(\omega)$), energy-loss function ($L(\omega)$), and refractive index ($n(\omega)$) It exhibited the same optical character for the polarization states indicated by [010] and [100], while the polarization state indicated by [001] showed a divergent behavior in all properties.

IV. SHIELDING EFFECT (SE) PERFORMANCE OF Fe_2B

The electromagnetic shielding efficiency (SE) of Fe_2B, which exhibits ferrimagnetic behavior as a member of the P4/mmm space group in 2D tetragonal crystalline structure, has been investigated in the spectrum range of 31.558-123980 nm allowed by the morphological properties of the material. The SE efficiency has been investigated separately for the ultraviolet (UV), visible, and infrared (IR) regions for [001], [010] and [100] polarization states. The total shielding efficiency (SE_T) is analyzed as the sum of the reflection-induced shielding efficiency (SE_R) and absorption-induced shielding efficiency (SE_A), while the shielding efficiency caused by multiple internal reflections (SE_M) [20], which has a very low effect, is neglected.

Figure 10 shows the reflection (SE_R), absorption (SE_A), and total (SE_T) shielding efficiency of monolayer Fe_2B material in the ultraviolet spectrum (31.558-388.284 nm).

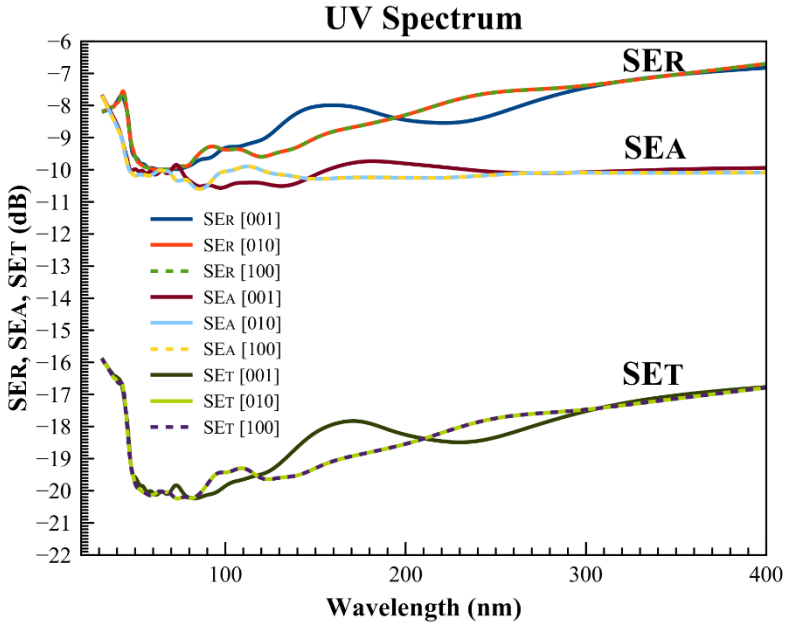

Figure10. *SER, SEA, SET performances in the UV spectrum of Fe2B at [001], [010] and [100] polarization states*

The maximum SE_R, SE_A, and SE_T values of Fe_2B in the UV spectrum are shown in Table 2.

Table 2. *Maximum SER, SEA, and SET values in the UV spectrum.*

UV Spectrum (31.558-388.284 nm)			
dB	Max. SER	Max. SEA	Max. SET
[001]	-9.999	-10.565	-20.239
[010]	-10.000	-10.601	-20.243
[100]	-10.000	-10.609	-20.243

Figure 11 shows the reflection (SE_R), absorption (SE_A) and total (SE_T) shielding efficiency of monolayer Fe_2B material in the visible spectrum (390.688-746.661 nm).

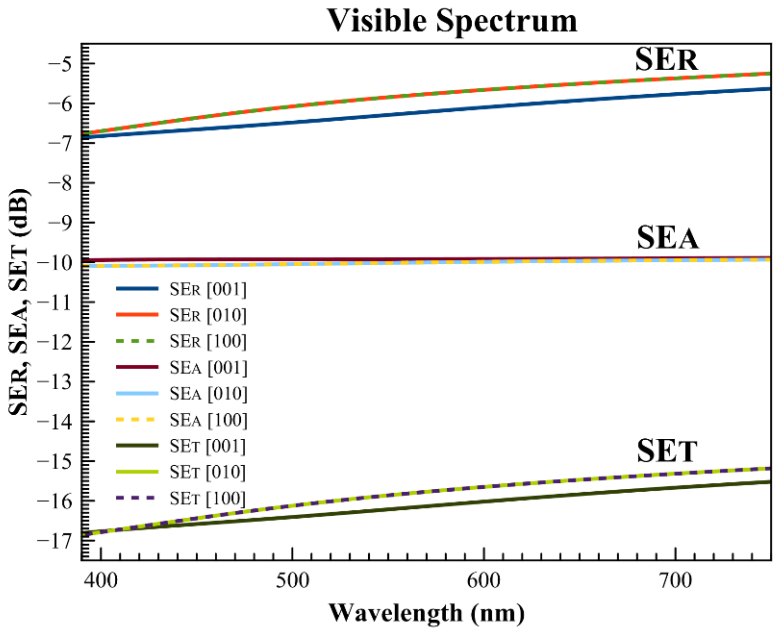

Figure11. *SER, SEA, SET performances in the visible spectrum of Fe2B at [001], [010] and [100] polarization states*

The maximum SE_R, SE_A and SE_T values of Fe_2B in the visible spectrum are shown in Table 3.

Table 3. *Maximum SE_R, SE_A and SE_T values in the visible spectrum.*

Visible Spectrum (390.688-746.661 nm)			
dB	Max. SER	Max. SEA	Max. SET
[001]	-6.860	-9.947	-16.807
[010]	-6.763	-10.089	-16.852
[100]	-6.763	-10.089	-16.852

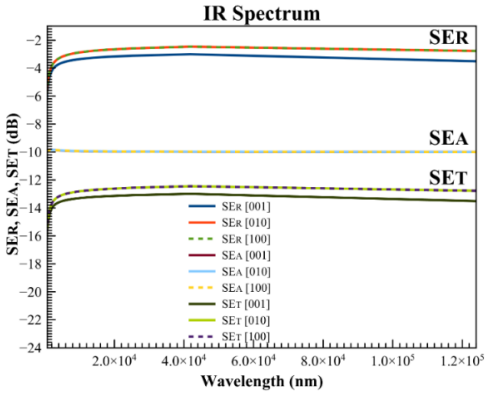

Figure12. *SER, SEA, SET performances in the infrared spectrum of Fe2B at [001], [010] and [100] polarization States*

The maximum SE_R, SE_A and SE_T values of Fe_2B in the infrared spectrum are shown in Table 4.

Table 4. *Maximum SE_R, SE_A and SE_T values in the infrared spectrum.*

IR Spectrum (755.602-123980 nm)			
dB	Max. SER	Max. SEA	Max. SET
[001]	-5.617	-9.999	-15.504
[010]	-5.237	-9.998	-15.167
[100]	-5.237	-9.998	-15.167

The maximum values of SE_R, SE_A and SE_T efficiencies for the [001], [010] and [100] polarization states of 2D Fe2B with tetragonal crystal structure in the range of 31.558 -123980 nm are shown in dB in Figure 13.

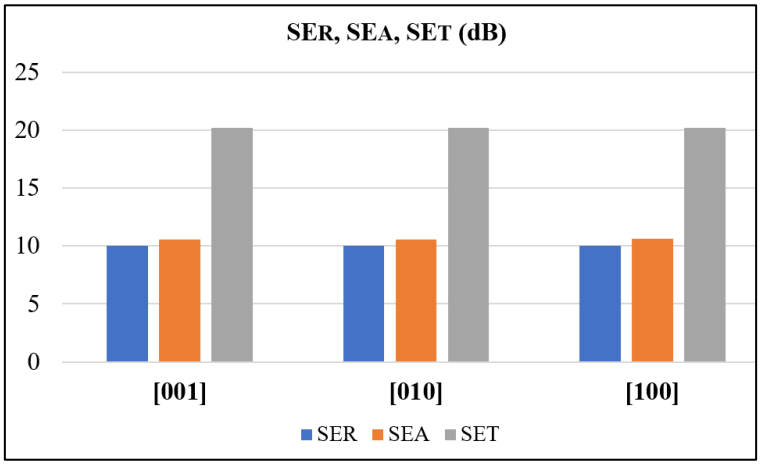

Figure 13. *SE effect of 2D Fe_2B material in the range 31.558-123980 nm*

Fe_2B exhibited shielding performance in the ultraviolet region, visible region, and infrared region with $SE_A > SE_R$ and showed absorptive-type shielding properties. Fe_2B started to show its shielding performance at wavelengths above 31,557 nm. At wavelengths up to 50 nm (within the NUV region), the material exhibited increasing shielding performance with the effect of absorption performance and then gradually decreasing shielding performance.

Although the SE_A, SE_R and SE_T shielding efficiencies of Fe_2B in the ultraviolet spectrum were the same in the [010] and [100] polarization states, the maximum SE_T was 20.243 dB, while the maximum SE_T performance in the [001] polarization state was 20.239 dB, 0.02% lower.

Fe_2B exhibited an absorptive shielding performance in the visible spectrum with $SE_A > SE_R$. While the SE_A performance for Fe_2B does not show a significant change in this region, the SE_R performance tends to decrease. This effect resulted in a loss of total shielding efficiency (SE_T) performance at wavelengths further away from the visible spectrum. Fe_2B showed the highest total shielding efficiency of 16.852 dB at [010] and [100] polarization states, with the absorption-induced shielding efficiency (SE_A) being greater than the reflection-induced shielding efficiency (SE_R).

Fe_2B exhibited shielding performance in the infrared region with $SE_A > SE_R$, indicating absorptive-type shielding. While the SE_A performance for Fe_2B does not show a significant change in this region, the

SE_R performance tends to decrease. This effect resulted in a loss of total shielding effectiveness (SE_T) performance at wavelengths further away from the visible region. Although the total shielding performances (SE_T) at [010] and [100] polarization states were the same, the maximum SE_T value at [001] polarization state was 15.504 dB.

The 2D material obtained using Fe_2B nanoparticles behaved as an absorptive type shielding material in [001], [010] and [100] polarization states and exhibited the maximum SE_T performance (>20 dB) in the UV spectrum.

When the literature on 2D-based electromagnetic shielding materials is examined, the EMI shielding performances (SE) of the materials shown in Table 5. are remarkable despite their ultra-thin structures.

Table 5. *SE performance of selected 2D based materials in thickness and frequency ranges.*

Material	**Loading**	**Thickness (d) (mm)**	**EMI SE (dB)**	**Frequency (GHz)**	**Reference**
Graphene film	bulk	0.25	17	12.4–18	[35]
Graphene paper	bulk	0.050	60	8.2-12.4	[36]
Graphene film	bulk	0.015	20.2	1-4	[37]
Multilayer graphene	bulk	0.018	55	12-18	[38]
Graphene aerogel	bulk	2	20	12.4-18	[35]
Flexible Graphite	bulk	3.1	130	1-2	[39]
rGO film	bulk	0.0084	19.1	8-12	[40]
Ti_3CNT_x	film (100 wt%)	0.04	116.0	8.2-12.4	[41]
$Ti_3C_2T_x$	film (100 wt%)	0.01	70.0	8.2-12.4	[42]
$Ti_3C_2T_x$-ANF	film (90.9 wt%)	0.01	34.7	8.2-12.4	[43]
TiO_2-$Ti_3C_2T_x$/GO	bulk	0.0091	28.2	12.4	[44]
$Mo_2Ti_2C_3T_x$	film	0.0035	26	8.2–12.4	[45]
$Mo_2TiC_2T_x$	film	0.004	23	8.2-12.4	[45]
MoS_2/glass	30 wt%	1.5	24.2	8.2-12.4	[46]
BP-GO	film (50 wt%)	0.01	29.7	8-12	[47]
GO-h-BN-polymer	film	0.24	37.9	8.2-12.4	[48]
Fe_2B	DFT	bulk sheet	20.243	$4.083X10^6$	This work

In the study conducted by Tripathi et al. [35], they reported the SE performance of the 0.25 mm thick bulk structure graphene film at 12–18 GHz as 17 dB. In the study by Zhang et al. [36], the SE

performance of 0.050 mm thick graphene paper material in bulk structure was reported as 60 dB in the frequency range of 8.2-12.4 GHz. In another study conducted by Kumar et al. [37] on a bulk graphene film, the SE performance of the 0.015 mm thick material in the 1-4 GHz range was measured as ~20 dB. The 0.018 mm thick bulk material using multilayer graphene by Paliotta et al. [38] demonstrated 55 dB SE performance for 12-18 GHz. Singh et al. [35] reported that the SE performance of 2 mm thick graphene aerogel is 20 dB in the range of 12.4-18 GHz. In the study by Luo and Chung [39], the SE performance of 3.1 mm thick flexible graphite material in bulk structure was reported as 130 dB for 1-2 GHz. In another study by Sehen et al. [40], the 0.0084 mm thick bulk material obtained using rGO film showed ~19 dB SE performance for 8-12 GHz. In their study [41], Iqbal et al. reported the SE performance of the 0.04 mm thick material obtained using Ti_3CNT_x in film (100 wt%) structure as 116 dB under 8.2-12.4 GHz. In another study [42], Han et al. reported the SE performance of the 0.01 mm thick material obtained by using $Ti_3C_2T_x$ in film (100 wt%) structure as 70 dB at 8.2-12.4 GHz. In their study [43], Wei et al. showed that the SE performance of the 0.01 mm thick material obtained using $Ti_3C_2T_x$-ANF in film (90.9 wt%) structure was 34.7 dB at 8.2-12.4 GHz. In the study conducted by Xiang et al. [44], the bulk structured TiO_2-$Ti_3C_2T_x$/GO with a thickness of 0.0091 mm showed an SE performance of 28.2 dB at 12.4 GHz. Shahzad et al [45] reported the SE performance of 0.0035 mm thick $Mo_2Ti_2C_3T_x$ film at 8.2-12.4 GHz as 26 dB. In the same study, Shahzad et al. [45] reported the SE performance of 0.004 mm thick $Mo_2TiC_2T_x$ film at 8.2-12.4 GHz as 23 dB. Wen et al. [46] reported that the SE performance of 1.5 mm thick MoS_2/glass at 30 wt% filler ratio was 24.2 dB below 8.2-12.4 GHz. In their study [47], Zhou et al. showed that the SE performance of the 0.01 mm thick material obtained by using BP-GO in film structure (50 wt%) was 29.7 dB at 8-12 GHz. In their study [48], Zhang et al. showed that the SE performance of 0.24 mm thick 11-layer film-structured GO-h-BN-polymer material at 8.2-12.4 GHz is ~38 dB. In this study, where the DFT method was used, the SE performance of 2D Fe_2B in monolayer structure in the frequency range of 4.083X106 GHz was determined as 20.243 dB.

V. CONCLUSION

The structural, electronic, magnetic and optical properties of Fe_2B in the P4/mmm space group in the tetragonal crystal structure have been theoretically investigated using the DFT method on a quantum mechanical basis using ab initio methods, followed by a detailed study of the SE performance of the 2D film material obtained using Fe_2B unit cells. The electromagnetic shielding efficiency of the electromagnetic wave (radiation) penetrating into the material from the [001], [010], [100] directions of the monolayer Fe_2B film material with a tetragonal crystal structure showing ferrimagnetic properties was investigated using ab-inito methods. Monolayer Fe_2B exhibited the best shielding performance (SE_T) of 20.243 dB in the ultraviolet region in the [010] and [100] cases where the radiation was perpendicular to the material. Neglecting the shielding effect caused by multiple internal reflections (SE_M), 10.6 dB of this performance is due to the absorption effect (SE_A) and 10 dB to the refractive effect (SE_R). The shielding response of the material started at 31.558 nm and lasted until 123980 nm. This performance is remarkable considering the morphological properties of the two-dimensional (2D) material. The SE_T performance (>20 dB) of Fe_2B, a member of the MBene family, is exciting for the use of 2D materials in electromagnetic shielding.

VI. REFERENCES

[1] D. Bor, (2015) "Radyasyon nedir?" Halkımız için bilgilendirme kılavuzu Ankara Üniversitesi Fizik Mühendisliği Bölümü [Çevrimiçi]. Erişim: http://www.radkorder.org/wp-content/upload/2016/09/RADYASYON NED%C4%BOR.pdf

[2] Y. E. Togay, "Radyasyon ve biz," *Türkiye Atom Enerjisi Kurumu Yayınları*, c. 2, s. 12, 2002.

[3] A. Türkkan, O. Çerezci ve K. Pala, *Elektromanyetik Alan ve Sağlık Etkileri*, Bursa, Türkiye: F. Özsan Matbaacılık, 2012.

[4] A. Balmori, "Electromagnetic pollution from phone masts. Effects on wildlife," *Pathophysiology*, vol. 16, no. 2-3, pp. 191-199, 2009.

[5] P. Bandara and D. O. Carpenter, "Planetary electromagnetic pollution: it is time to assess its impact," *The Lancet Planetary Health*, vol. 2, no. 12, pp. e512-e514, 2018.

[6] F. Çerezci, "K-means algoritması ile elektromanyetik kirlilik analizi," Bilgisayar ve Bilişim Mühendisliği, Yüksek lisans tezi, Sakarya Üniversitesi, Sakarya, Türkiye, 2015.

[7] G. Redlarski, B. Lewczuk, A. Zak, A. Koncicki, M. Krawczuk, J. Piechocki, K. Jakubiuk, P. Tojza, J. Jaworski, D. Ambroziak, L. Skarbek and D. Gradolewski "The influence of electromagnetic pollution on living organisms: historical trends and forecasting changes," *BioMed Research International*, vol. 2015, no. 1, pp. 234098, 2015.

[8] O. Elmas, "Effects of electromagnetic field exposure on the heart: a systematic review," *Toxicology and Industrial Health*, vol. 32, no. 1, pp. 76-82, 2016.

[9] A. Ahlbom and M. Feychting, "Electromagnetic radiation: environmental pollution and health," *British Medical Bulletin*, vol. 68, no. 1, pp. 157-165, 2003.

[10] L. Cui, Y. Wang, X, Han, P. Xu, F. Wang, D. Liu, H. Zhao and Y. Du "Phenolic resin reinforcement: a new strategy for hollow NiCo@ C microboxes against electromagnetic pollution," *Carbon*, vol. 174, pp. 673-682, 2021.

[11] R. Yılmaz, "Elektromanyetik kalkanlama özelliği olan malzemeler," *Electronic Journal of Vocational Colleges*, vol. 4, no. 1, pp. 136-150, 2014.

[12] M. Altun, İ. Karteri, M. Güneş, and M. H. Alma, "Grafen katkılı odun-plastik nanokompozitlerinin elektromanyetik özellikleri ve elektromanyetik kalkanlama etkinliği karşılaştırmalı çalışması," *Kahramanmaraş Sütçü İmam Üniversitesi Mühendislik Bilimleri Dergisi*, c. 20, s. 1, ss. 38-47, 2017.

[13] L. Chhaya, "EMR pollution-an imperceptible threat for safety," *SSRN*, 2165743, 2012.

[14] S. Ghosh, S. Ganguly, P. Das, T.K. Das, M. Bose, N.K. Singha, A.K. Das and N. Ch. Das, "Fabrication of reduced graphene oxide/silver nanoparticles decorated conductive cotton fabric for high performing electromagnetic interference shielding and antibacterial application," *Fibers and Polymers*, vol. 20, pp. 1161-1171, 2019.

[15] A. Kaşgöz, "Elektromanyetik dalga kalkanlama özelliğine sahip polimer kompozitlerin geliştirilmesi ve yapı-performans ilişkilerinin incelenmesi," Doktora tezi, Kimya Mühendisliği Bölümü, İstanbul Üniversitesi, İstanbul, Türkiye, 2017.

[16] V. Shukla, "Review of electromagnetic interference shielding materials fabricated by iron ingredients," *Nanoscale Advances*, vol. 1, no. 5, pp. 1640-1671, 2019.

[17] E. Zornoza, G. Catalá, F. Jiménez, L. G. Andión, and P. Garcés, "Electromagnetic interference shielding with Portland cement paste containing carbon materials and processed fly ash," *Materiales de Construcción,* vol. 60, no. 300, pp. 21-32, 2010.

[18] R. Çelen and Y. Ulcay, "Baryum Titanatin Tekstilde Elektromanyetik Kalkanlama Uygulamalarında KullanIMI," *Uludağ Üniversitesi Mühendislik Fakültesi Dergisi*, c. 23, s. 2, ss. 29-44, 2018.

[19] A. Iqbal, P. Sambyal, and C. M. Koo, "2D MXenes for electromagnetic shielding: a review," *Advanced Functional Materials*, vol. 30, no. 47, pp. 2000883, 2020.

[20] M. González, J. Pozuelo, and J. Baselga, "Electromagnetic shielding materials in GHz range," *The Chemical Record*, vol. 18, no. 7-8, pp. 1000-1009, 2018.

[21] P. Banerjee, Y. Bhattacharjee, and S. Bose, "Lightweight epoxy-based composites for EMI shielding applications," *Journal of Electronic Materials*, vol. 49, pp. 1702-1720, 2020.

[22] S. Geetha, K. Satheesh Kumar, C. R. Rao, M. Vijayan, and D. Trivedi, "EMI shielding: Methods and materials—A review," *Journal of Applied Polymer Science*, vol. 112, no. 4, pp. 2073-2086, 2009.

[23] H. W. Ott, *Electromagnetic Compatibility Engineering*, vol. 11, New Jersey, USA: John Wiley & Sons, 2011, pp. 423–459.

[24] H. Liu, A.T. Neal, Z. Zhu, Z. Luo, X.Xu, D. Tomanek and P. D. Ye, "Phosphorene: an unexplored 2D semiconductor with a high hole mobility," *ACS Nano*, vol. 8, no. 4, pp. 4033-4041, 2014.

[25] B. Anasori, M. R. Lukatskaya, and Y. Gogotsi, "*2D metal carbides and nitrides (MXenes) for energy storage*," in MXenes: Jenny Stanford Publishing, 2023, pp. 677-722.

[26] M. Naguib, O. Mashtalir, J. Carle, V. Presser, J. Lu, L. Hultman, Y. Gogotsi and M. W. Barsoum, "Two-dimensional transition metal carbides," *ACS Nano*, vol. 6, no. 2, pp. 1322-1331, 2012.

[27] Z. Jiang, P. Wang, X. Jiang, and J. Zhao, "MBene (MnB): a new type of 2D metallic ferromagnet with high Curie temperature," *Nanoscale Horizons*, vol. 3, no. 3, pp. 335-341, 2018.

[28] T. Zhang, B. Zhang, Q. Peng, J. Zhou, and Z. Sun, "Mo 2 B 2 MBene-supported single-atom catalysts as bifunctional HER/OER and OER/ORR electrocatalysts," *Journal of Materials Chemistry A*, vol. 9, no. 1, pp. 433-441, 2021.

[29] J. P. Perdew, K. Burke, and M. Ernzerhof, "Generalized gradient approximation made simple," *Physical Review Letters*, vol. 77, no. 18, pp. 3865, 1996.

[30] B. Hammer, L. B. Hansen, and J. K. Nørskov, "Improved adsorption energetics within density-functional theory using revised Perdew-Burke-Ernzerhof functionals," *Physical Review B*, vol. 59, no. 11, pp. 7413, 1999.

[31] S. J. Clark, M. D. Segall, C. J. Pickard, P. J. Hasnip, M. I. J. Probert, K. Refson and M.C. Payne, "First principles methods using CASTEP," *Zeitschrift Für Kristallographie-Crystalline Materials*, vol. 220, no. 5-6, pp. 567-570, 2005.

[32] E. Engel and R. M. Dreizler, *Density Functional Theory*, vol. 2, 1st ed., Springer Vertag, Berlin: pp. 11-56, 2011.

[33] K. Momma and F. Izumi, "VESTA 3 for three-dimensional visualization of crystal, volumetric and morphology data," *Journal of Applied Crystallography*, vol. 44, no. 6, pp. 1272-1276, 2011.

[34] G. Kumar, *Crystal Fıeld Theory: Analyzıng Molecular Structures and Properties*, A Textbook of Objective Inorganic Chemistry, 2022 (Revised) ed. vol. 12, New Delhi India: Wisdom Pres, 2022, pp. 86-93.

[35] S. Singh, P. Tripathi, A. Bhatnagar, Ch. R. P. Patel, A. P. Singh, S. K. Dhawan, B. K. Gupta and O. N. Srivastava, "A highly porous, light weight 3D sponge like graphene aerogel for electromagnetic interference shielding applications," *RSC Advances*, vol. 5, no. 129, pp. 107083-107087, 2015.

[36] L. Zhang, N. T. Alvarez, M. Zhang, M. Haase, R. Malik, D. Mast and V. Sahanov, "Preparation and characterization of graphene paper for electromagnetic interference shielding," *Carbon*, vol. 82, pp. 353-359, 2015.

[37] P. Kumar, F. Shahzad, S. Yu, S. M. Hong, Y.-H. Kim, and C. M. Koo, "Large-area reduced graphene oxide thin film with excellent thermal conductivity and electromagnetic interference shielding effectiveness," *Carbon*, vol. 94, pp. 494-500, 2015.

[38] L Paliotta, G. D. Bellis, A. Tamburrano, F. Marra, A. Rinaldi, S.K. Balijepalli, S. Kaciulis and M. S. Sarto, "Highly conductive multilayer-graphene paper as a flexible lightweight electromagnetic shield," *Carbon*, vol. 89, pp. 260-271, 2015.

[39] X. Luo and D. Chung, "Electromagnetic interference shielding reaching 130 dB using flexible graphite," *MRS Online Proceedings Library*, vol. 445, pp. 235-238, 1996.

[40] B. Shen, W. Zhai, and W. Zheng, "Ultrathin flexible graphene film: an excellent thermal conducting material with efficient EMI shielding," *Advanced Functional Materials*, vol. 24, no. 28, pp. 4542-4548, 2014.

[41] A. Iqbal, F. Shahzad, K. Hantanasırısakul, M. Kım, J. Kwon, J. Hong, H. Kım, D. Kım, Y. Gogotsi and C. M. Koo, "Anomalous absorption of electromagnetic waves by 2D transition metal carbonitride Ti3CNT x (MXene)," *Science*, vol. 369, no. 6502, pp. 446-450, 2020.

[42] M. Han, C. E. Shuck, R. Rakhmanov, D. Parchment, B. Anasorı, C. M. Koo, G. Friedman and Y. Gogotsi, "Beyond Ti3C2T x: MXenes for electromagnetic interference shielding," *ACS Nano*, vol. 14, no. 4, pp. 5008-5016, 2020.

[43] H. Wei, M. Wang, W. Zheng, Z. Jiang, and Y. Huang, "2D Ti3C2Tx MXene/aramid nanofibers composite films prepared via a simple filtration method with excellent mechanical and electromagnetic interference shielding properties," *Ceramics International*, vol. 46, no. 5, pp. 6199-6204, 2020.

[44] C. Xiang, R. Guo, S. Lin, S. Jiong, J. Lan, C. Wang, C. Cui, H. Xiao and Y. Zhang, "Lightweight and ultrathin TiO2-Ti3C2TX/graphene film with electromagnetic interference shielding," *Chemical Engineering Journal*, vol. 360, pp. 1158-1166, 2019.

[45] F. Shahzad, M. Alhabeb, C. B. Hatter, B. Anasorı, S. M. Hong, C. M. Koo and Y. Gogotsi, "Electromagnetic interference shielding with 2D transition metal carbides (MXenes)," *Science*, vol. 353, no. 6304, pp. 1137-1140, 2016.

[46] Q. Wen, W. Zhou, J. Su, Y. Qing, F. Luo, and D. Zhu, "High performance electromagnetic interference shielding of lamellar MoSi2/glass composite coatings by plasma spraying," *Journal of Alloys and Compounds*, vol. 666, pp. 359-365, 2016.

[47] T. Zhou, H. Ni, Y. Wang, C. Wu, H. Zhang, J. Zhang, A. P. Tomsia, L. Jiang and Q, Cheng, "Ultratough graphene–black phosphorus films," *Proceedings of the National Academy of Sciences*, vol. 117, no. 16, pp. 8727-8735, 2020.

[48] X. Zhang, X. Zhang, M. Yang, S. Yang, H. Wu, S. Guo and Y. Wang, "Ordered multilayer film of (graphene oxide/polymer and boron nitride/polymer) nanocomposites: an ideal EMI shielding material with excellent electrical insulation and high thermal conductivity," *Composites Science and Technology*, vol. 136, pp. 104-110, 2016.